

Positron Annihilation Techniques Suited for Porosity Characterization of Thin Films

M. P. Petkov,^{*,†} C. L. Wang, M. H. Weber, and K. G. Lynn

Department of Physics, Washington State University, Pullman, Washington 99164-2814

K. P. Rodbell

IBM T.J. Watson Research Center, P.O. Box 218, Yorktown Heights, New York 10598

Received: October 25, 2001; In Final Form: October 30, 2002

The porosity in thin ($\sim 1\ \mu\text{m}$) mesoporous low dielectric constant (low- k) films is investigated by different beam-based positron annihilation spectroscopy (PAS) techniques. Examples are given for mesoporous methyl-silsesquioxane films deposited with a sacrificial polymer (porogen, from 0 to 90 wt % load) and subsequently annealed to drive out the volatile porogen, resulting in films with nanometer size voids. The important features of positronium (Ps; an electron–positron atom-like bound state) interaction with porous materials (formation, confinement, diffusion, thermalization, and annihilation) are highlighted. Ps was identified as an especially suitable probe for identifying open porosity, manifested by Ps escape in a vacuum. Three-photon (3γ) PAS was utilized to derive the length-scale for pore interconnectivity prior to total percolation, and open porosity fraction as a function of the porogen load. Lifetime spectroscopy (PALS) was used to obtain the pore size distribution, and the Ps energy is assessed using the momentum-sensitive PAS techniques. For the mesoporous low- k films, these two complementary techniques yield the vast majority of the porosity properties assessable by PAS. The necessity for future improvements in the PAS analysis, as well as a broad-scale comparison with other diagnostic techniques is discussed.

I. Introduction

Over the past two decades, the performance improvements in microelectronic devices have been achieved mainly through miniaturization of device components. To realize future progress, however, the semiconductor industry has been forced to undergo an historic evolution, adopting the use of new materials to lower the signal propagation delay between devices ($R \times C$, where R is interconnect line resistance, C is the dielectric capacitance).¹ While the replacement of Al with less resistive Cu is underway, the successful integration of a material for use as an interlayer dielectric (ILD) with a dielectric constant (low- k , $k < 2.5$) has not yet been achieved in mass production. A large number of sol–gel materials, organic and inorganic polymers, etc., are presently being evaluated; however, it is widely accepted that to produce ultralow- k dielectrics ($k \leq 2.0$), embedded pores will be required (since air has a $k \approx 1.0$). To this end, different methods for producing mesoporous (pore size $> 1\ \text{nm}$) dielectric films have been developed (e.g., for porous methyl-silsesquioxane (MSSQ), see ref 2).

A detailed knowledge of the porosity properties, such as fraction, size distribution, morphology, etc., is essential for choosing the best ILD material, which can be successfully integrated. The porosity is studied by a number of widely used techniques (small-angle X-ray scattering, small-angle neutron scattering, gas absorption techniques, ellipsometric porosimetry, electron microscopy, etc.), and recently by positron annihilation spectroscopy (PAS).^{3–10}

PAS is a nondestructive technique for the characterization of open-volume defects in materials (from vacancies to voids).^{11,12}

The local electronic environment determines the annihilation characteristics (lifetime, number of annihilation photons, and transferred momentum) of positrons in a sample. Four PAS techniques or variants are available: (1) positron annihilation lifetime spectroscopy (PALS), (2) Doppler broadening (DB), (3) angular correlation (ACAR), and (4) 3-photon Ps decay (3γ). These focus on different properties of the annihilation photons to obtain complementary information about the electronic environment.¹¹ Of all of the PAS variants, PALS is the most common and is widely used for studying porosity properties in bulk polymers,^{13,14} including MSSQ.¹⁵ Most of the ILD candidates, however, are prepared as thin films ($\sim 1\ \mu\text{m}$), for which the bulk PAS methods are inadequate. Monoenergetic positron beams¹¹ are needed to inject positrons at shallow depths. The inherent depth-profiling capability of beam-based PAS opens up a new dimension in the low- k research, namely the ability to depth profile through a thin film.^{6,7,9,10,16}

In this paper, we address Ps interactions in porous thin films. The processes of Ps formation, confinement in pores, diffusion, thermalization, and annihilation are discussed in the context of the porosity properties in mesoporous thin films. Recipes are presented for using different PAS variants to obtain information on pore size distribution, open porosity fraction, pore interconnectivity, and total percolation.

II. Background

In insulators, a positron may form positronium (Ps), a hydrogen-like bound state with an electron. In mesoporous films, Ps is the ideal pore-sensitive PAS probe, as opposed to positrons, since Ps annihilation characteristics depend strongly on pore size in the relevant porosity range ($> 1\ \text{nm}$).

1. Ps Formation, Trapping, and Kinetics. Ps formation in solids has been described by two models—Øre¹⁷ and spur-

* Corresponding author.

[†] Present address: Jet Propulsion Laboratory, California Institute of Technology, 4800 Oak Grove Drive, Pasadena, CA 91109.

electron capture.^{18,19} Their respective role in solids has much been debated^{20,21} (see, e.g., the detailed discussion given in the Appendix). The different spatial dependence of the Ps formation with respect to a solid/vacuum interface (e.g., pore surface), defined by these two models is relevant to this work. The Øre model allows for strong Ps formation, whereas the spur Ps formation is suppressed at surfaces. The mesoporous films studied here exhibit experimental evidence for a competition between these two models, each contributing to the Ps signal (see Appendix). Ps can be formed at a pore surface or in the solid, from where it can diffuse to a pore.

Positron and Ps diffusion processes in a mesoporous sample determine a “sensitivity volume” around a pore, where implanted positrons can form Ps, which, in turn, can probe the pore. The positron diffusion length in nonporous MSSQ is of the order of 10 nm (this varies moderately with curing conditions¹⁶). The Ps diffusion length in a variety of organic and inorganic amorphous solids is reported to be ~ 1 nm.²²

Ps entering a void lowers its zero-point energy, converting the difference into kinetic energy (up to a few eV), which gradually dissipates during inelastic interactions with the void walls. After losing only a fraction of its initial energy, even epithermal Ps ($E \gg kT$) is no longer able to re-enter the solid and remains confined to the pore volume. Although Ps tunneling between pores has been suggested in theory,²³ it has been argued that it is restricted by a small mismatch in the Ps energy levels in the pores.^{24,25} However, connected pores forming clusters allow Ps motion on a larger length-scale. Therefore, both thermal and epithermal Ps can escape from the sample finding a route through an open channel to the sample surface. This defines the use of the terms *open* and *closed* pores for PAS—where an open pore is a pore or a cluster of pores, which facilitates Ps escape from the film, whereas the latter defines a closed pore. It is worth noting that interconnected pores, sealed from the vacuum surface by a capping layer, are seen as closed porosity.

2. Ps Annihilation. Ps initially forms in two states, para- p -Ps ($\uparrow\downarrow$ electron–positron spin configuration) and ortho- o -Ps ($\uparrow\uparrow$), whose annihilation characteristics are drastically different. The annihilation rate of Ps in a vacuum is set by the overlap of the electron and positron wave functions and their spin configuration. For opposite spins, p -Ps ($\uparrow\downarrow$), the annihilation occurs predominantly via two photons (2γ), with a rate of $\sim 8 \times 10^9$ s⁻¹. The 2γ -channel is forbidden for parallel spins ($\uparrow\uparrow$)—because angular momentum cannot be conserved—leading to a dominant higher-order 3γ -annihilation process, with a significantly smaller rate, $\sim 7 \times 10^6$ s⁻¹. The resulting p -Ps and o -Ps lifetimes in a vacuum are 0.125 ns and 142 ns,²⁶ respectively. The p -Ps lifetime changes little in solids,¹⁷ whereas the o -Ps lifetime is shortened by the so-called “pick-off” (2γ) annihilation with molecular electrons of opposite spin to that of the positron, and spans 2 orders of magnitude (~ 1 –142 ns). For example, values of 2.5–3.5 ns are reported for sub-nanometer voids in unfoamed MSSQ,¹⁵ and 20–100 ns were measured in foamed MSSQ.^{3–9} Utilizing this broad range, positron annihilation lifetime spectroscopy (PALS) has emerged as a powerful tool for measuring the pore size in bulk polymers^{13,14} and thin films.^{3–10,27} Theoretical models establishing the relation between Ps lifetime and pore size in sub-nanometer pores^{28–30} have been extended to larger pore sizes.^{3,4,8,31} These relations enable pore size distributions to be deduced from the distributions of Ps lifetimes, obtained by Laplace inversion of PALS spectra (numerical routines CONTIN^{32,33} and MELT^{34,35}).

For 2γ -annihilation, the energy and momentum conservation laws restrict the individual photon energies to be 511 keV plus

Doppler red/blue shifts, with the angle between the photons close to 180°. Due to the extra degree of freedom in a 3γ -event, the individual photon energies have only an upper limit (511 keV). This allows the construction of a 3γ -to- 2γ annihilation ratio,¹¹ which can be calibrated to measure the fraction of 3γ Ps annihilations.^{36,37} The 3γ signal depends on both void size and density, and, for bulk studies, carries no novel information in comparison to PALS. However, as will be demonstrated below, the 3γ depth-profiling of mesoporous films probes void connectivity, and yields complementary information to PALS.

The PALS and 3γ techniques are insensitive to the momentum of the annihilating positron-electron pair, which is measured by either DB or ACAR. This information is important for the assessment of the Ps energy in a pore, which depends on the energy exchange rate and the collision rate with the walls. The temperature dependence of the o -Ps lifetime—pore size correlation,^{3,4} implies a corresponding energy dependence of the 3γ Ps decay, since the pick-off rate in a pore determines the 3γ -to- 2γ annihilation ratio. It should be noted, however, that a comparison with experimental data⁸ suggested that o -Ps in mesoporous materials is thermalized.

The (2γ) annihilation of epithermal p -Ps and/or pick-off o -Ps may cause large Doppler shifts of the photon energies, which shapes the annihilation line in the same way as thermal positron annihilations with high-momentum electrons. Thus, the Doppler line shape parameter¹¹ (S), which characterizes annihilation with small Doppler shifts, would decrease with an increase in the Ps energy (under otherwise identical conditions). Epithermal Ps annihilation can be expected for p -Ps escaping from the film (due to the lack of any energy loss mechanism outside the film), and for o -Ps pick-off annihilation in pores. A simple simulation for 5 nm voids shows that the degree of Ps thermalization depends on the energy-loss mechanism. Assuming an energy loss rate of the order of 1 meV/collision (typical for phonons), the time for thermalization is compatible with the p -Ps lifetime. Negligible thermalization times are obtained for average rates of as high as 100 meV/collision. Although such energy loss processes are available (e.g., molecular bond excitation), they occur rarely and contribute little to the average rate. Therefore, p -Ps almost certainly annihilates prior to achieving thermal equilibrium with the medium.

The correlation of the 3γ and S profiles of the mesoporous films provides insight into the pore interconnectivity and degree of Ps thermalization in the closed pores, which may affect the interpretation of the PALS results. ACAR can be used to measure the p -Ps energy and void size, as well as to detect residual anisotropy in the porosity.³⁸

III. Experiment

A monoenergetic positron beam with a rate of $\sim 2 \times 10^5$ e⁺/s and tunable energy was used in conjunction with a conventional DB/ 3γ system and a PALS spectrometer, constructed in separate sections of a shared beam line. A high-efficiency high-purity Ge detector with energy resolution of 1.45 keV at 514 keV (⁸⁵Sr γ -line) was used for the DB/ 3γ measurements; spectra with $1\text{--}2 \times 10^6$ events were accumulated at each beam energy. The ratio of the integral counts within a ~ 1.5 keV window, centered at 511 keV, and the total photopeak area was used to analyze the shape of the annihilation line. This so-called “shape”, or S -parameter,¹¹ depicts the annihilation of low-momentum positron–electron pairs, causing small Doppler shifts of the emitted photons. Conversely, the ratio of the counts in the 2–4.5 keV from the centroid on both sides and the photopeak makes the so-called “wing”, or W -parameter,¹¹ depicting high-

momentum annihilation. The S - and W -values are normalized to unity for defect-free Si to eliminate systematic effects (resolution and integration windows). The full energy spectra were used to determine the 3γ -to- 2γ annihilation ratio,¹¹ which is independent of both S and W and measures the self-annihilation of Ps from its triplet state (o -Ps). The 3γ -to- 2γ ratio was calibrated to measure the 3γ Ps decay fraction.^{36,37}

The lifetime apparatus, described in detail elsewhere,^{39,40} is an experimental clock, measuring the time intervals between positron impact on the sample, and its annihilation with an electron. A "start" signal was provided by the secondary electrons, formed at positron impact, collected by a channel electron multiplier array. A CsF scintillator in conjunction with a photomultiplier tube (PMT) was used to detect the annihilation radiation. The timing resolution of the system was ~ 0.5 ns in a time window of ~ 1.3 μ s. PALS spectra containing at least 10 million counts were collected in two different PMT configurations for each sample. In the first, the PMT detected annihilation events within and outside the film (escaped Ps through connected pores), whereas in the second, an absorber (γ -shield) was used to restrict the PMT acceptance angle from the sample. The two configurations are used here to detect Ps escape from the film as in ref 5. The spectra taken with the γ -shield, which are not influenced by Ps decay outside the film, were analyzed to obtain information on pore sizes.

The samples for these studies were ~ 0.7 μ m-thick porous MSSQ films, fabricated using a sacrificial porogen technique.² Si wafers were spin-coated with a solution containing low molecular weight MSSQ resin with from 0 to 90 wt % pore generator (porogen) additions. This blend was cured in a 300 Torr N_2 ambient. Initially, the temperature was ramped to 200 °C to achieve vitrification of the MSSQ network (formation of MSSQ-porogen nanohybrid). In a second annealing step at 450 °C the porogen decomposed and was driven out of the film. The final morphology of the porosity (pore size and distribution) is related to the morphology of the MSSQ-porogen nanohybrid. The total porosity is proportional but not equal to the porogen load. Results from refractive index measurements⁴¹ yielded a factor of 0.77 ± 0.01 (porosity = $0.77 \times$ porogen load) for the MSSQ-porogen system studied.

IV. Results

The decomposition of the sacrificial porogen has been one method used to monitor void formation. Infrared (IR) spectroscopy gives evidence of porogen decomposition by virtue of the relative intensity of the 1725 cm^{-1} peak (characteristic of the porogen carbonyl stretch) as a function of temperature.² Dynamic measurement of the peak intensity as a function of the temperature is presented in Figure 1a (data from ref 2).

The IR data are compared to PAS parameters from measurements of a set of 20 wt % porogen samples, cured isochronally at 200 °C, 243 °C, 292 °C, 350 °C, 400 °C, and 450 °C. Figure 1b shows the DB low-momentum (S) parameter (open symbols) and the 3γ o -Ps decay at 2 keV beam energy (solid symbols). The S data are the characteristic values for each film, determined as in ref 16. A Boltzmann fit to these data shows a transition temperature of 318 ± 1 °C with the width of the transition (full width at half-maximum of the derivative) being 50 ± 0.5 °C. A strong change in the 3γ signal is also seen in that temperature region. This figure shows the direct link between the porogen decomposition (as seen by IR) and the appearance of voids (as seen by PAS).

The experimental 3γ depth-profiles for fully cured MSSQ films made with 0–90 wt % porogen loads are shown in Figure

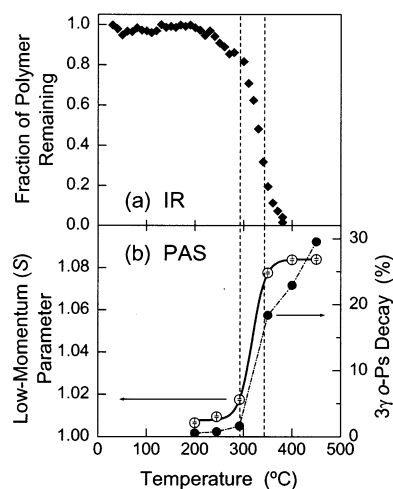


Figure 1. Porogen decomposition and void formation in a MSSQ–20 wt % porogen nanohybrid. (a) Infrared spectroscopy shows porogen decomposition by the decreased intensity of the 1725 cm^{-1} peak (from ref 2). (b) PAS shows void formation (bottom) by the change in the DB low-momentum (S) parameter (open circles) and 3γ o -Ps decay (solid circles). The vertical lines mark the porogen decomposition region, determined from the PAS data (see text).

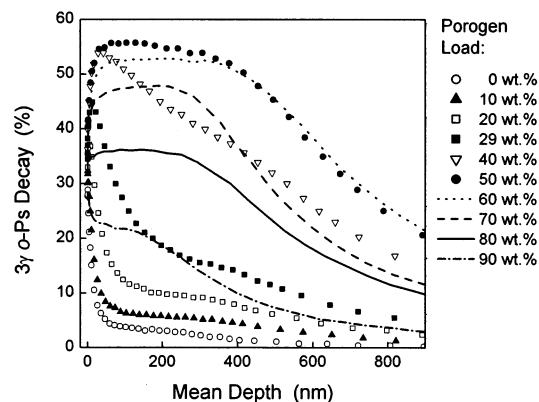


Figure 2. Experimental depth-profiles of the 3γ o -Ps annihilation fraction for films with different porogen load.

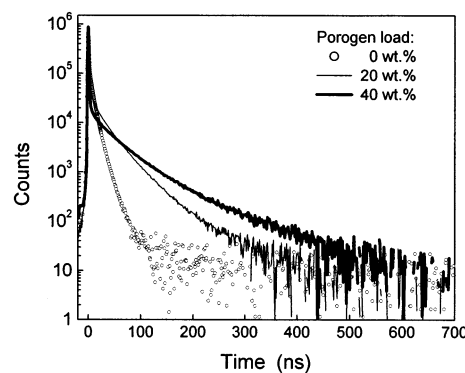


Figure 3. Typical PALS spectra of MSSQ films with, containing 10^7 counts (constant background subtracted; peak-to-background ratio was 7000:1).

2. Initially, the 3γ -Ps signal in the film follows the increase in porosity (symbols); however, the opposite trend is observed for highly porous films (lines). The curvatures of these profiles are used to derive the length-scale for Ps motion in the pores, while the characteristic 3γ -values are used to obtain the open porosity fraction.

Figure 3 shows typical PALS spectra of unfoamed (0 wt %) and foamed (20 wt % and 40 wt % porogen loads) MSSQ films,

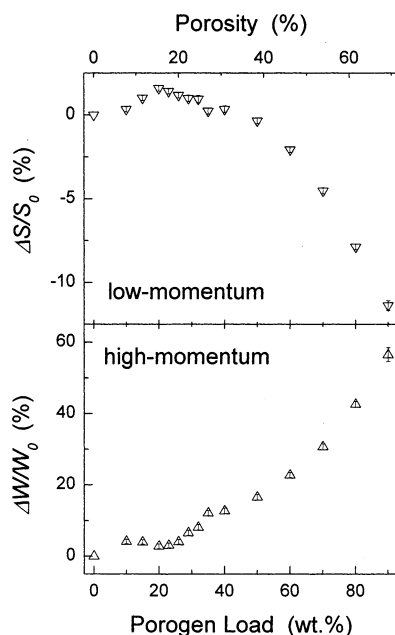


Figure 4. Changes in the 2γ low-momentum (S) and high-momentum (W) annihilation parameters versus porogen load, given as $(X - X_0)/X_0$, where X_0 is the respective MSSQ parameter. The vertical line at 25 wt % porogen load marks the pore interconnectivity threshold.

with subtracted constant background. In addition to the ~ 4 ns Ps lifetime, typical for the cages in the MSSQ network,¹⁵ the unfoamed sample exhibited a ~ 10 ns lifetime with a smaller but comparable intensity to that of the 4 ns lifetime. This corresponds to a pore size of approximately 1.7 nm, which is present in all samples independent of porogen content.

Depth-profiles of the Doppler parameters (S and W) were acquired simultaneously with the 3γ -signal. The characteristic values for each film were normalized to the MSSQ value (of the unfoamed film), and the differences with respect to that are shown in Figure 4. The positron–electron annihilation from a p -Ps, which is in thermal equilibrium with the solid, carries negligible momentum. Due to that, the introduction of porosity in the MSSQ films causes an increase in S and a decrease in W , seen at small porogen loads. For highly porous films, however, the trend is the opposite. It will be shown that the large Doppler shifts, responsible for the observed changes in S and W , result from the annihilation of energetic Ps.

V. Analysis and Discussion

The porosity, at which an open-to-closed cell transition occurs, is an important characteristic for any mesoporous dielectric material. o -Ps is sensitive to this transition, because it can travel a much longer distance than the typical pore diameter, and can escape from a film (MSSQ is otherwise impermeable to Ps trapped in pores). The probability for o -Ps escape from an open pore in MSSQ is near unity; within its typical lifetime, Ps traverses a path length on the order of 0.1–1 cm,^{3,4} while the film thickness is typically less than 1 μ m. Therefore, Ps escape from a film can be used to measure open porosity, defined by the permeability of the film to atomic Ps gas. This definition arises from the similarity with conventional gas-absorption techniques; however, the major difference is that Ps is equally sensitive to both open and closed pores, the latter of which are “invisible” in a gas-absorption experiment.

1. Diffusion Model. The behavior of Ps in pores can be described classically as a percolation process. Because of the similarity between percolation and diffusion,⁴² we find the

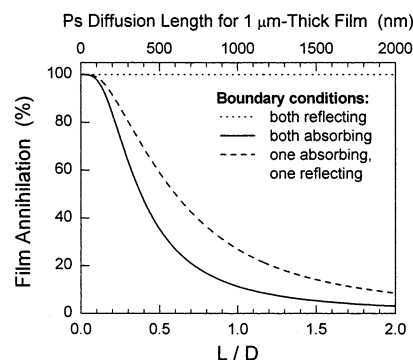


Figure 5. Fraction of Ps annihilating in a film as a function of the diffusion length (L) in units of film thickness (D), L/D . Ps with a $\tau = 50$ ns lifetime is initially implanted at $D/2$ and the diffusion coefficient is calculated as L^2/τ . The top scale shows diffusion length for 1 μ m-thick film.

discussion of a simple one-dimensional diffusion model beneficial to the understanding of the experimental results. This model solves the diffusion equation for one special case of initial conditions, where Ps is created with an infinitely narrow distribution in the center of a layer of thickness D . Since this model is intended as a guide to the results, we do not consider the actual shape of the positron implantation profiles^{43,44} and the resulting initial Ps concentration across the film. The diffusion equation

$$\frac{\partial n(x,t)}{\partial t} = D_{\text{Ps}} \nabla^2 n(x,t) - \frac{1}{\tau} n(x,t)$$

is solved for a fixed Ps lifetime ($\tau = 50$ ns; corresponding to ~ 4 nm voids^{3,4}), and a diffusion coefficient, $D_{\text{Ps}} = L^2/\tau$, for a given diffusion length, L . The fraction of Ps annihilation in the film, f_{Ps} , is then calculated as a function of L (in units of film thickness, L/D) for all combinations of totally absorbing or totally reflecting boundary conditions (Figure 5).

The trivial solution for two reflecting boundaries (Figure 5, dotted line) is given to illustrate that a film with interconnected channels (large L), sealed at both interfaces with a solid MSSQ layer is indistinguishable from a film with isolated pores ($L \sim 0$) with a diameter similar to the channels cross-section. Therefore, Ps annihilation at the film interface must yield different characteristics from that at the pore walls for open porosity to be measured. Then, f_{Ps} depends strongly on L , as shown for the cases with one (solid line) and two absorbing boundaries (dashed line); in the latter case, the maximum change occurs at $L/D = 0.25$. Figure 5 also predicts no depth-dependence of the annihilation parameters for films in which Ps is confined in isolated pores (e.g., $L/D < 0.01$; $L \sim$ pore diameter).

The most realistic scenario for these MSSQ films is given by the two absorbing boundaries. One of them corresponds to the film/vacuum interface, through which Ps can escape from the film. The other absorbing boundary represents the SiO_2 layer at the film/substrate (Si) interface, at which the fast pick-off Ps annihilation results in a loss of 3γ -signal. It is evident, that when L becomes compatible to D , the conditions at both boundaries will strongly influence the measurement of the characteristic 3γ -signature of a film. This can be demonstrated by using the model to reproduce the shape of the experimental 3γ depth profiles.

Initially (at a given beam energy), Ps is created at depth z in a film with a thickness D , whose boundaries are perfect absorbers. We equate the intensity of the 3γ -signal to the total

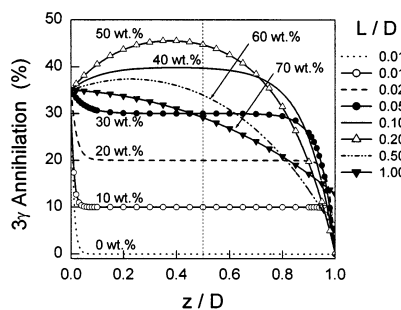


Figure 6. Simulated 3γ annihilation profiles for films with 0–70 wt % porosity versus initial Ps formation depth in film thickness units, z/D (see text for details). The initial Ps profile is a δ -function, and the diffusion length (L/D) increases as shown. The two perfectly absorbing boundaries at $z/D = 0$ and $z/D = 1$ have 35% and 0% 3γ signatures, respectively.

porosity, thus ignoring the fact that only a fraction of the Ps in closed pores annihilates in a 3γ -process. Further, we assume (somewhat arbitrarily) that 35% of the 3γ -annihilation occurs at the film surface, and 0% at the substrate (an excellent approximation for the SiO_2 -covered Si⁴⁵). To simulate Ps escape from interconnected pores, we allow the Ps escape length (or diffusion length) to grow exponentially at above 20% porosity. Such a scenario can occur if the porosity is comprised of identically sized pores, whose connectivity is determined solely by statistical probability. The results of these 3γ depth-profile models are shown in Figure 6, where units of film thickness are used both for the depth scale, z/D , and for the diffusion length, L/D .

Despite being excessively simplified, this diffusion model (Figure 6) reproduces the basic features observed experimentally (Figure 2). The results for porosities $< 20\%$, for which the Ps escape length is short (such as for positron and Ps diffusion; see Section II), the surface and film signals are easily identified and no change is observed throughout the film thickness. The increase of L at higher porosity ($\geq 40\%$) mimics the depth-dependence of the 3γ -profile. The film 3γ -value is not achieved for porosities $> 50\%$. More importantly, the measured 3γ -signal apparently decreases at even higher porosity, due to the longer Ps escape length, which decreases the chance of Ps annihilation in the film.

2. 3γ -PAS. 2.1. Closed-to-Open Cell Transition and Cluster Size. To calculate the length-scale characterizing the Ps motion in the mesoporous MSSQ films we used standard software for the analysis of positron data (VEPFIT⁴⁶). This model accounts for the shape of the positron implantation profiles, and for positron and Ps diffusion in the matrix. The positron diffusion length, L_+ , calculated from both S and W depth-profiles as in ref 16, was approximately 10 nm, and changed marginally as a function of porosity. The “Ps diffusion length” (in the terms of the diffusion model), L , was calculated from the 3γ -profiles. Since positrons implanted at depths of the order of L_+ may diffuse back to the vacuum interface and form Ps there, the value of L needs to be corrected for positron diffusion in order to represent the Ps escape length, L_{esc} . An exact treatment would involve coupled diffusion equations, in which the sources of Ps diffusing in the pores are (1) Ps formed by diffusing positrons in the bulk and subsequently diffusing to the pores, and (2) Ps formed at pore walls. A simplification is given by $L^2 = L_{\text{esc}}^2 + L_+^2$, which overestimates the influence of positron diffusion. However, this is an acceptable approximation since one is interested in the changes in L_{esc} due to connected pores (interconnectivity), as opposed to obtaining an absolute value for L_{esc} .

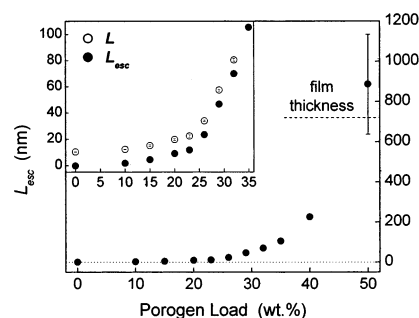


Figure 7. Ps escape length, L_{esc} , as a function of the porogen load. For films in which the Ps escape length is compatible with the film thickness (dashed line at 720 nm), the calculation error is large. The inset shows L_{esc} in an enlarged window, alongside L (open circles), the calculated value before correction for the diffusion in the solid. The threshold for pore interconnectivity at ~ 25 wt % porogen load is evident in both sets of data.

Figure 7 shows the calculated L_{esc} as a function of porogen load ≤ 50 wt %. Above ~ 25 wt % porogen load (inset), L_{esc} increases more rapidly with porogen load than below 25 wt %. We identify this critical porogen load value as the *pore interconnectivity threshold* (closed-to-open cell transition). The increased Ps escape length above the connectivity threshold is significantly larger than the typical pore sizes [4–10 nm, derived from X-ray and neutron scattering experiments (unpublished) and from PALS (below)], yet much smaller than the film thickness. This implies that the pore connectivity threshold for these samples lies below the percolation threshold, at which a pore cluster spanning the entire film is formed, and Ps escape from any depth is possible.

The pore connectivity threshold can be determined from L alone, without considering positron diffusion; Figure 7 shows that the sharp change in both L and L_{esc} occur at the same porogen load. The corrected values (L_{esc}), however, give a better representation of the length-scale of Ps motion. We attribute these values of L_{esc} to the average size of the pore clusters connected to the surface, assuming that these are homogeneously and isotropically distributed in the film. (For asymmetric pore clusters oriented anisotropically with respect to the surface normal, L_{esc} characterizes the direction normal to the surface). Knowing the typical cluster size in a film allows one to determine the density of interconnected pores and, e.g., to assess the risk of forming a “killer pore cluster” linking two neighboring metal interconnect lines in an electronic device.

2.2. Open Porosity Fraction. The open and closed porosity fractions in a film determine its characteristic 3γ -value. For small porogen loads, this is the asymptotic (“bulk”) level of the 3γ -profiles (Figure 2). For highly porous films, however, the experimentally measured “bulk” 3γ -signal is influenced by Ps escape through the film surface, pick-off annihilation at the bottom interface, and, possibly, the suppressed (spur) Ps formation. As indicated by the diffusion model, this effect can be significant for $L/D > 0.1$ (Figure 5), which in these samples occurs around 30 wt % (see Figures 7 and 2). Therefore, when calculating the “bulk” 3γ -values,⁹ care has to be taken to properly account for Ps percolation through the open pores.

Figure 8 shows $\Delta 3\gamma$, the “bulk” 3γ -values as a function of porogen load after correction for the 3γ -annihilation in the MSSQ network, which amounts to 2.6% in the film without porogen addition. Thus, the $\Delta 3\gamma$ values represent the mesopores in the films. It is apparent that for porogen loads > 60 wt % the films are too thin to accurately determine their characteristic 3γ -values (as well as Ps escape length; e.g., see Figure 7). The Ps annihilation in closed pores carries the convoluted informa-

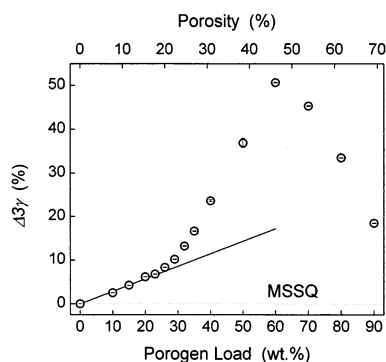


Figure 8. The change in the 3γ *o*-Ps annihilation with respect to the MSSQ value (no porogen added) as a function of the porogen load. A line fit to the data for <25 wt % porogen load is extrapolated to 60 wt %.

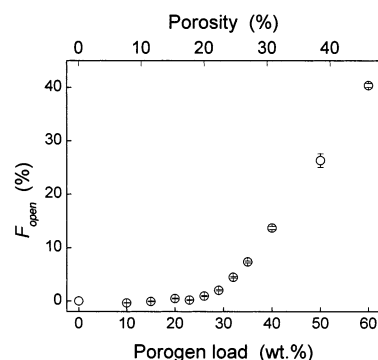


Figure 9. Escaped Ps fraction, identified as the open porosity fraction, F_{open} , as a function of the porogen load.

tion on pore size and density in a given film, and yields, $3\gamma_{\text{film}}$. This value could be measured experimentally in the absence of Ps escape. Conversely, escaped Ps can only undergo self-annihilation, giving a signal $3\gamma_{\text{esc}} = 100\%$. In our experimental setup, the escaped Ps drifts away, thus suppressing the efficiency for its detection, which we estimated to be $\sim 91\%$ for Ps with energy $E = kT$, and $\sim 80\%$ for $E = 0.1$ meV. Being uncertain of the Ps energy, we ignore this loss of 3γ signal for the calculation below (this results in a simple scaling factor of the results). Thus, each “bulk” 3γ -value, $3\gamma_{\text{bulk}}$ (Figure 8, <60 wt % porogen load), is composed of the annihilation of escaped Ps and Ps in the pores, whose contributions are weighted with the respective fractions of open and closed porosity, F_{open} and $F_{\text{closed}} = 1 - F_{\text{open}}$:

$$3\gamma_{\text{bulk}} = F_{\text{open}} \times 3\gamma_{\text{esc}} + F_{\text{closed}} \times 3\gamma_{\text{film}}$$

To obtain the $3\gamma_{\text{film}}$ -values at high porosity, we assume that they depend linearly on the porogen load. A fit to the $\Delta 3\gamma$ data for <25 wt % porogen load (Figure 8) yields a $0.288 \pm 0.001\%$ 3γ -signal for each percent of porogen load. Thus, F_{open} , shown in Figure 9, is calculated from the 3γ profiles (Figure 2). In agreement with the pore interconnectivity threshold, determined from the Ps escape length, the open porosity fraction increases at above 25 wt % porogen load. Therefore, both L_{esc} and F_{open} are sensitive to the open-to-close cell transition as a function of porosity (porogen load).

3. PALS. 3.1. Mean Pore Size and Pore Size Distribution. The first moment (mean lifetime) is a unique characteristic of a PALS spectrum. Its value, however, is dominated by the short lifetime components (due to annihilation of positrons, *p*-Ps, and *o*-Ps in the MSSQ cages), and is therefore unsuitable for the derivation of pore sizes. A mean *o*-Ps lifetime, $\bar{\tau}_{o-\text{Ps}}$, can be

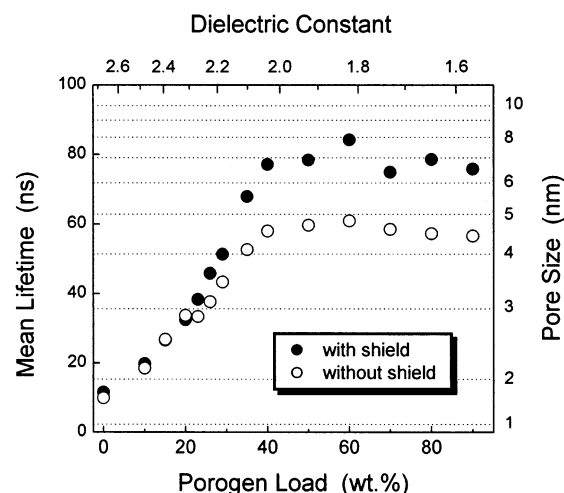


Figure 10. Mean *o*-Ps lifetime as a function of porogen load, calculated from spectra taken with (open circles) and without a γ -shield (solid circles). The open symbols relate to the mean pore size in the films (right scale, from ref 8), keeping in mind that for long channels PALS is more sensitive to its cross-section than its length.

defined from the first moment after the influence of short lifetime components are eliminated. To this end, for a given spectrum, $N(t)$, we calculate the first moment for $N(t > t_c)$ as a function of t_c , where t_c is a cutoff time. From this we determine the minimum t_c , required to obtain a stable $\bar{\tau}_{o-\text{Ps}}$ (not affected by short lifetimes). Figure 10 shows $\bar{\tau}_{o-\text{Ps}}$ as a function of porogen load, for the two γ -detector configurations; e.g., see Section III. The difference in $\bar{\tau}_{o-\text{Ps}}$ for the two detection schemes identifies the Ps escape in a vacuum,⁵ where its annihilation (lifetime ~ 142 ns) results in increased values of $\bar{\tau}_{o-\text{Ps}}$. The pore connectivity threshold seen by PALS is at ~ 23 wt % porogen load, which is in fair agreement with the 25 wt % value determined by 3γ -PAS.

The measured Ps lifetime in samples containing open porosity will be reduced from the characteristic for the pores value due to the Ps escape rate. However, a comparison between spectra of capped and uncapped identical MSSQ films⁵ taken with the γ -shield suggested that this reduction is experimentally insignificant.⁵ Because of that, the values of $\bar{\tau}_{o-\text{Ps}}$ (Figure 10, open circles) can be related to the mean pore size in the film (left scale; from ref 8). It must be stressed that for elongated pores (channels), PALS is more sensitive to their cross-section than to their length. Thus, we attribute the 4.5–5 nm saturation value for porogen loads greater than 50 wt % to the cross-section of the highly connected pore network (similar to that determined using the 3γ -PAS spectra).

The pore size distribution(s) in the mesoporous samples are obtained from the PALS spectra taken with the γ -shield. In this work, we (1) use the maximum entropy routine (MELT) to obtain *o*-Ps lifetime distribution(s) through the inverse Laplace transformation of the PALS spectra, and (2) convert these to pore size distribution(s) using the relationship from ref 8. The ~ 4 ns and ~ 10 ns lifetimes originating from the MSSQ network were detected in all spectra. To minimize their influence on the determination of the size of the porogen-induced pores, we used in the analysis only the delayed events, which occur after some time t_0 (i.e., data for which $t > t_0$). For each spectrum, the value of t_0 was chosen as the minimum delay, for which the first moment of the analyzed portion of the spectrum remained unchanged. The respective t_0 values were approximately: 10 ns for 0–35 wt %; 15 ns for 40 wt %; 20 ns for 50–70 wt %; and 25 ns for 80–90 wt % porogen load.

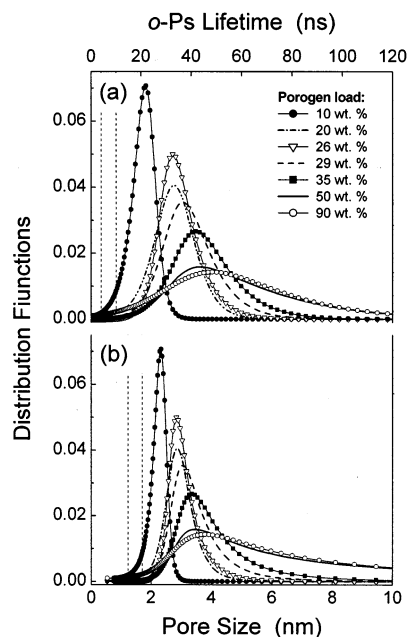


Figure 11. (a) Positron lifetime distribution functions for MSSQ films with different porogen loads. The dashed vertical line marks the lifetimes (4 ns and 10 ns) in the MSSQ matrix, which are common for all samples regardless of the porogen load. (b) The corresponding pore size distribution using the calibration from ref 8.

Naturally, the shorter lifetimes in the less porous samples dominate the MSSQ lifetimes and allow for shifting t_0 to lower values. Figure 11 shows the results for typical cases of the sample set: (a) gives the area-normalized *o*-Ps lifetime distribution, and (b) gives the corresponding pore size distribution. Both the ~ 4 ns and ~ 10 ns lifetimes (dashed lines) in the MSSQ network (not shown) are left out for clarity.

The conversion from lifetime to pore size is worth discussing. In ref 8, the *o*-Ps lifetime is correlated with the Ps mean free path, and not the pore size. Thus, a pore shape *must* be assumed to translate l into the more conventional term — pore size. For Figure 11b, we assumed a spherical pore shape, whose diameter was used as a measure of pore size. With that in mind, the pore size distributions for samples with mostly isolated pores (porogen loads ≤ 25 wt %) are a good representation of the actual porosity. Conversely, for samples with highly interconnected pore structures (50–90 wt % porogen load), the deviation from the spherical shape is significant. This is evident from the appearance of a tail at the higher end of the distribution. A more detailed model, considering simultaneously the size distribution from PALS and escape length from 3γ -PAS is needed in order to construct a generalized picture of the porosity for samples containing both isolated and connected pores.

Exponential functions (representing lifetimes) comprise a nonorthogonal matrix in which a PALS spectrum is resolved. Therefore, two or more lifetime components are not always resolved uniquely due to correlation between the parameters (lifetimes and intensities). As an example, the PALS spectra of all samples (for $t > 30$ ns, excluding the short lifetimes) are equally well represented mathematically ($\chi^2 \approx 1$) by two discrete exponential functions ($\exp[-(t/\tau)]$), and by a single stretched exponential function ($\exp[-(t/\tau)^\beta]$). These results translate, respectively, into a *narrow bimodal*, and a *broad monomodal* pore size distribution. Thus, the derivation of the actual representation of the porosity requires care. It should be noted that the results for the mean pore size (from $\bar{\tau}_{o-Ps}$) are unambiguous.

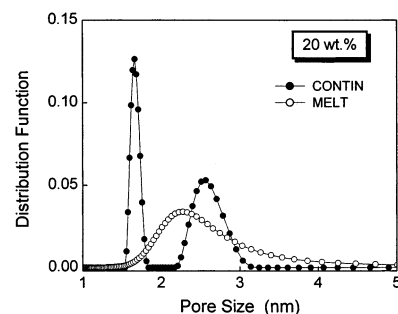


Figure 12. Pore size distribution for a MSSQ film with 20 wt % porogen load. Positron lifetime distributions were obtained from the same data set, using different software for performing inverse Laplace transformation (CONTIN vs MELT). The results were converted to pore size distributions using ref 8. CONTIN analysis consistently yields bimodal distribution for all samples, in contrast to X-ray scattering experiments.

Apart from this fundamental mathematical problem, the capability of the two commonly used routines for PALS inverse Laplace transformation, CONTIN and MELT, to accurately represent the sample porosity has long been debated.^{47–49} The criteria for the separation of two lifetimes in close proximity have also been addressed.⁴⁹ Furthermore, epithermal Ps annihilation (if existing) can cause additional broadening or splitting of the *o*-Ps lifetime distribution.⁵⁰ It should also be stressed that comparison of the two routines was done predominantly for nanometer-sized pores (1–3 ns lifetimes), whereas more research is warranted for mesoporous materials (long 10–100 ns lifetimes).

In Figure 12 we show a comparison of the pore size distributions in the 20 wt % sample, obtained by CONTIN (solid symbols) and MELT (open symbols). These calculations are based on the same range of data ($t > 20$ ns) from the same data set. The mean lifetimes obtained with these two routines are similar. The pore size distributions, however, are drastically different, which has a severe impact on the deduced porosity structure. Extensive tests were conducted on simulated PALS spectra to evaluate the feasibility of applying CONTIN and MELT to extract long lifetime distributions. We found that CONTIN, in its present form, tends to break a broad input distribution into several narrow peaks, thus artificially producing multimodal distributions. In our judgment, CONTIN is unsuitable for research on mesoporous materials (exhibiting 20–100 ns lifetimes). MELT, however, produces satisfactory results. For a reference, small-angle X-ray scattering experiments yielded broad monomodal distributions for these samples;⁵¹ however, the technique may not be sensitive to the smaller pores in the MSSQ. Conversely, they may be observable by ellipsometric porosimetry, which has given bimodal distributions on similar samples.⁵²

3.2. Depth-Profiling of Pore Size Distribution. PALS studies have not yet taken a full advantage of the depth-profiling capabilities of low-energy positron beams. Collected at a chosen positron implantation depth, each PALS spectrum contains region-averaged information on the porosity, analogous to a *single point* in a 3γ -profile (Figure 2). To date, there are no PALS fitting routines, analogous to VEPFIT⁴⁶ intended for Doppler and 3γ spectra. This hampers PALS ability to utilize the knowledge of positron implantation profiles, and to probe the cluster connectivity, as well as Ps and positron diffusion properties.

Figure 13 shows a PALS depth-profile for a sample made with 20 wt % porogen load, created from 13 individual high-statistics (10^8 events) spectra, collected at different positron

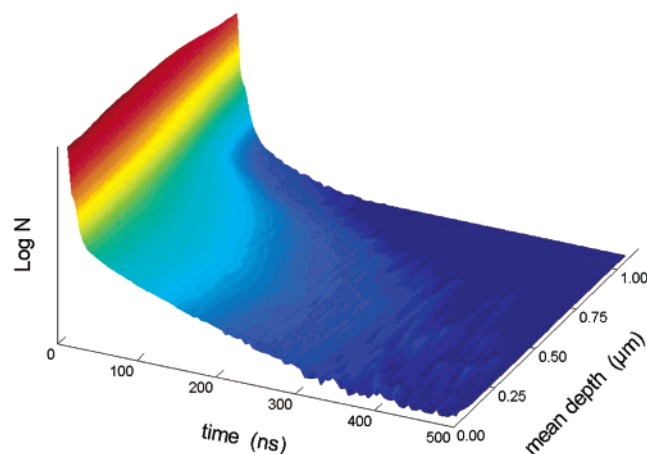


Figure 13. PALS depth-profile of a film with 20 wt % porogen load, created from 13 spectra, collected at approximately equidistant steps in depth. The strong change in the long lifetime at the film–substrate interface ($\sim 0.7 \mu\text{m}$) originates from the *o*-Ps annihilation within the film, and the lack of Ps formation in the substrate.

implantation depths (beam energies) without using the γ -shield. This figure is the PALS analogue of the 3γ -profiles, shown in Figure 2, and Doppler profiles (not shown here). An intense long-lifetime component is present throughout the film, and vanishes upon implantation of the positrons into the Si substrate (at $\sim 0.7 \mu\text{m}$), much like the 3γ -profiles (Figure 2). The interpretation of the lifetime distribution in each individual PALS spectrum can benefit from knowledge of the trends at each mean depth (e.g., knowing the spectra at shallower and deeper depths), especially when two lifetimes appear close. This can be achieved by an inverse Laplace transformation routine (analogous to CONTIN and MELT), which uses the depth information in a manner similar to VEPFIT.

4. Ps Energy. The pore sizes and size distributions under consideration assume that *o*-Ps in pores is in thermal equilibrium with the solid. To achieve higher accuracy in representing the porosity, an assessment of the Ps energy is necessary.^{8,50} Figure 4 also hints at the significance of such an assessment, by showing an increased high-momentum annihilation (low *S*, high *W*) at high porosity. Energetic *p*-Ps cannot explain this due to an insufficient amount formed. Considering this in conjunction with the 3γ -PAS results and the diffusion model, we conclude that the *o*-Ps pick-off annihilation at the bottom MSSQ/SiO₂ interface occurs with a significantly higher rate compared to MSSQ. Since identically sized pores in bulk MSSQ and SiO₂ exhibit the same *o*-Ps lifetime,^{8,31} the fast pick-off rate at the interface could be attributed to the local electronic environment there. The Doppler data contain the relevant information; however, the evaluation of the Ps energy from them is not trivial. This is due to the large number of events, which contribute to the *S* and *W* parameters, and the limited resolution of the detectors.

Ps energy assessment from the annihilation of *p*-Ps may be more promising. The feasibility of a two-dimensional (2D) ACAR system to address this issue has been shown previously.³⁸ 2D-ACAR has significantly better momentum resolution than Doppler systems, and it is virtually insensitive to 3γ -annihilation. *p*-Ps escaping from the film causes a net momentum, directed away from the surface, which is measured by 2D-ACAR and can be used to calculate the Ps energy. Alternatively, the red Doppler shift due to *p*-Ps drifting away (i.e., detector behind sample) can be detected by monitoring the centroid of the annihilation line. An example of the red Doppler shift caused

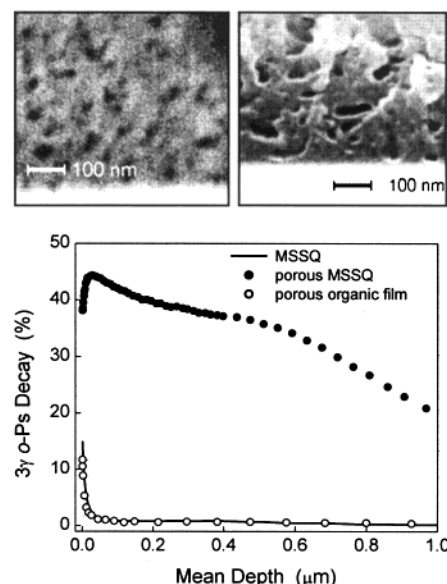


Figure 14. Material dependence of the *o*-Ps annihilation signature. An inorganic and an organic film (top left and right FE-SEM pictures, respectively) exhibit similar pore sizes, however, the *o*-Ps annihilation signature is drastically different (bottom). The 3γ signal in the organic film (open circles) is similar to that of nonporous MSSQ (line), showing no indication of large pores.

by moving positrons in an electric field is shown in ref 53. We constructed a similar setup, in which the centroid of the annihilation peak was measured with respect to a reference ¹³⁷Cs γ -source. A sample with 50 wt % porogen load was measured at 1 keV (high Ps formation, large probability for escape) and 30 keV (positrons are implanted into the Si substrate; no Ps formation occurs). The *p*-Ps escape was confirmed by the resulting 38 ± 2 eV red Doppler shift. The conversion of this value to Ps energy requires a careful evaluation of the contribution from all 2γ -annihilation events. Further research is warranted.

5. Chemical Dependence of the *o*-Ps Signatures. Most publications, as well as the discussion presented above, leave untreated some cases of Ps interaction with molecular electrons, which may drastically change the annihilation rate. Such examples are Ps quenching by paramagnetic centers,⁵⁴ chemical bonding of Ps,⁵⁵ etc. In the extreme case, Ps may be bound to the surface of a pore and not be sensitive to its open volume. Neglecting such Ps interactions can lead to enormous errors in evaluating pore sizes. Thus, the “survival” cross-section of Ps during a wall collision has to be considered as a material-dependent parameter and not, as done to date, as a universally constant cross section. A new organic thermosetting polymer provides an excellent example for the case of an enhanced annihilation rate. A comparison (Figure 14) of the FE-SEM cross-sections of this film and a film with ~ 30 wt % porogen shows large pores of similar size and concentration in both materials. The 3γ *o*-Ps signature in the organic polymer, however, is as small (open circles) as in unfoamed MSSQ (line), and much smaller than that of the porous MSSQ. The *o*-Ps lifetime in the organic polymer was ~ 2 ns, also similar to that of unfoamed MSSQ (~ 4 ns), and drastically different from the porous MSSQ (~ 63 ns). The fact that both positron and Ps diffusion (diffusion lengths calculated from 3γ PAS and Doppler spectra of the unfoamed materials) are similar implies that differences exist in the Ps–pore wall interactions for these two materials.

VI. Summary

In this work, we discussed the physics involved in Ps interaction with mesoporous dielectric materials. We utilized different PAS techniques to investigate the properties of thin mesoporous MSSQ films. 3γ *o*-Ps PAS was used to derive most of the information discussed, complemented by PALS as an option for obtaining pore size distributions. The 3γ *o*-Ps technique also benefits from a significantly faster acquisition rate than PALS (minutes versus hours). Additionally, it was noted that the assessment of the Ps energy by DB or ACAR facilitates further improvement in the accuracy of these results.

The attraction of Ps to pores makes it an ideal probe for void interconnectivity. Merged voids on a length-scale significantly smaller than the film thickness were detected by virtue of the Ps escape length, calculated from 3γ depth-profiles. Knowing the pore interconnectivity length is useful for assessing the probability of having large pore clusters, which could potentially link parallel metal wires in integrated circuits. Further, the pore interconnectivity threshold as a function of porogen load can be used to identify materials and processes, which shift this threshold to higher values.

The open porosity fraction was evaluated from the 3γ -values characterizing the "bulk" of the films, which were presented as a superposition of the contributions from escaped Ps and Ps annihilating in the film. The escaped Ps fraction was then equated to the open porosity fraction (assuming Ps to be a classical particle).

We evaluated the pore size distributions in mesoporous films by PALS, but cautioned that details of the lifetime analysis can render the decomposition of two or more lifetimes non-unique. In contrast, the relative comparison of films by means of a mean lifetime analysis can reliably identify trends. We also point out the need for the development of fitting routines (presently nonexistent), which utilize the depth-information in analogy to those available for 3γ and Doppler parameters. We constructed a PALS depth-profile and analyzed it in terms of continuous lifetime distributions, to point out the potential benefits of depth-profiling PALS.

Further improvement of the *o*-Ps lifetime–pore-size calibration requires the consideration of the material-dependence of the pick-off annihilation cross-section at the pore walls. While this has been overlooked, some examples have been found to deviate enormously from the common trend. To obtain a more accurate porosity picture by PAS, the Ps energy needs also to be assessed. Further, previously observed positron-irradiation-induced changes in the film⁵⁶ must also be evaluated carefully. Since changes were seen at a positron current density of as low as 1.5×10^{-9} A/m², resulting in a cumulative dose 10^8 – 10^9 times smaller than that of a typical SEM picture, the results from high-dose X-ray, electron, or neutron exposure experiments come into question.

In conclusion, this paper presents a recipe for using different PAS techniques to investigate the porosity characteristics of mesoporous dielectric films, establishing the 3γ *o*-Ps and PALS variants as the basis for such research. The cross-correlation of these results from the different PAS techniques helps to achieve a more complete picture of film porosity.

Acknowledgment. We thank W. Volksen and R. D. Miller (IBM Almaden Research Center) for supplying the samples used in this work, E. Huang and S. A. Cohen (IBM Watson Research Center) for SAXS, FE-SEM, and electrical measurements. This work was supported by the U.S. National Institute of Standards and Technology (NIST/ATP Cooperative Agreement No.

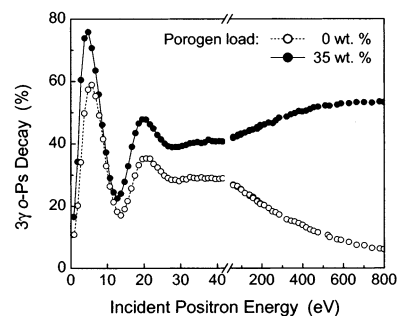


Figure 15. The 3γ *o*-Ps signal at low incident beam energy in an unfoamed MSSQ film (open symbols) and a film with 35 wt % porogen load (solid symbols).

70NANB8H4013), by the IBM T.J. Watson Research Center [Research Partnership Award (K.G.L.)], and by the DOE Basic Energy Sciences.

Appendix: Ps Formation Mechanisms

In the framework of the Øre model for solids,¹⁷ Ps formation is possible when the positron's energy is in excess of a required minimum, determined by the electronic properties of the material (electron ionization energy, Ps binding energy, Ps and positron work functions). This threshold energy determines the lower edge of the so-called Øre gap. An upper edge appears when the positrons have sufficient energy to excite electrons, in the process of which their energy is lowered below the lower edge of the Øre gap. The different electron ionization levels in a solid form different Øre gaps, which give rise to resonance-like features in the Ps signal as a function of positron energy. Low beam energy 3γ -data are shown in Figure 15 for an unfoamed and a foamed (35 wt % porogen load) film. The 0–50 eV region, where oscillations occur, is excluded from the depth-profiles in Figure 2; shown there are only the increase seen here at higher energies after the break. The oscillations in the Ps formation cross-section, governed by the Øre gaps in these films, are evident in the data.

The Øre model falls short in explaining the increasing Ps formation at higher beam energies (>50 eV; see also Figure 2), which is due to Ps formation by spur-electron capture. The spur model considers Ps formation from a positron, lacking energy for further ionization, which binds with an electron ionized during the positron cooling in the solid. With the increase of the incident energy, the Ps formation cross-section initially increases together with the free electron density in the proximity of the positron. Saturation occurs at some higher energy, when the positron thermalizes far from the area where the initial electron ionization occurred. The energy, which characterizes the saturation of the spur Ps formation process is known as terminal spur energy.¹⁸

Clearly, our experimental data contains evidence for coexisting Øre and spur Ps formation processes. Such coexistence has been demonstrated previously for ice,⁵⁷ whereas previously published results from PALS studies of thin polymer films²⁷ discarded the Øre model and establish the spur Ps formation. However, the lowest positron energy in these studies was 250 eV, well above the energy range in which the Øre-related effects are seen in this work.

With only spur Ps formation, it would be difficult to reconcile the strong Ps signal in aerogel- and xerogel-type samples with thin pore walls (e.g., density of 0.1–0.001 g/cm³). The measured terminal spur energy in the porous film was 0.36 ± 0.03 keV, from which the size of the MSSQ region, where the electron

spur is contained can be calculated. Hence, materials with pore walls thinner than approximately 10 nm will exhibit lower Ps formation cross-section.

Relative to the present work, the spur model carries a spatial dependence of the Ps formation, which is lower near surfaces due to the vanishing electron density in voids. In contrast, the Øre model is spatially independent (apart from differences in the electron ionization energies) and allows for Ps formation at the void surface. Scaling the PAS observables with the pore size cannot lead to a distinction between the two mechanisms, since both the Øre Ps formation at a pore surface and the trapping rate for bulk-formed spur Ps are proportional to the pore surface. We concur with the indication in the literature and in this work that the spur process probably dominates the Ps formation in most of the studied MSSQ films; however, further studies of highly porous materials are warranted.

References and Notes

- (1) International SEMATECH, *International Technology Road Map for Semiconductors*, 2001.
- (2) Hawker, C. J.; Hedrick, J. L.; Miller, R. D.; Volksen, W. *MRS Bull.* **2000**, 25, 54.
- (3) Gidley, D. W.; Frieze, W. E.; Dull, T. L.; Yee, A. F.; Ryan, E. T.; Ho, H.-M. *Phys. Rev. B* **1999**, 60, R5157.
- (4) Gidley, D. W.; Frieze, W. E.; Dull, T. L.; Sun, J.; Yee, A. F.; Nguyen, C. V.; Yoon, D. Y. *Appl. Phys. Lett.* **2000**, 76, 1282.
- (5) Petkov, M. P.; Weber, M. H.; Lynn, K. G.; Rodbell, K. P. *Appl. Phys. Lett.* **2000**, 77, 2470.
- (6) Petkov, M. P.; Weber, M. H.; Lynn, K. G.; Rodbell, K. P.; Volksen, W.; Miller, R. D. *Advanced Metallization Conference*, San Diego, October 3–5, 2000, in press (*MRS Symp. Proc.*).
- (7) Rodbell, K. P.; Petkov, M. P.; Weber, M. H.; Lynn, K. G.; Volksen, W.; Miller, R. D. *Mater. Sci. Forum* **2001**, 363–365, 15.
- (8) Dull, T. L.; Frieze, W. E.; Gidley, D. W.; Sun, J. N.; Yee, A. F. *J. Phys. Chem. B* **2001**, 105, 4657.
- (9) Petkov, M. P.; Weber, M. H.; Lynn, K. G.; Rodbell, K. P. *Appl. Phys. Lett.* **2001**, 79, 3884.
- (10) Uedono, A.; Chen, Z. Q.; Suzuki, R.; Ohdaira, T.; Mikado, T.; Fukui, S.; Shiota, A.; Kimura, S. *J. Appl. Phys. Lett.* **2001**, 90, 2498.
- (11) Schultz, P. J.; Lynn, K. G. *Rev. Mod. Phys.* **1988**, 60, 701.
- (12) Puska, M. J.; Nieminen, R. M. *Rev. Mod. Phys.* **1994**, 66, 841.
- (13) Jean, Y. C. *Mater. Sci. Forum* **1995**, 175–178, 59.
- (14) Yang, H.; Jean, Y. C. *Mater. Sci. Forum* **1997**, 255–257, 41.
- (15) Li, H.-L.; Ujihira, Y.; Yoshino, T.; Yoshino, K.; Yoshii, K.; Yamashita, T.; Horie, K. *Polymer* **1998**, 39, 4075.
- (16) Petkov, M. P.; Weber, M. H.; Lynn, K. G.; Rodbell, K. P.; Cohen, S. A. *Appl. Phys. Lett.* **1999**, 74, 2146.
- (17) Dupasquier, A. In *Positron Solid State Physics*, proceedings of the “Enrico Fermi” School summer course on “Positrons in Solids”, Varenna, Italy, 1981; Brandt, W., Dupasquier, A., Eds.; North-Holland: Amsterdam, 1983; p 510.
- (18) Mogensen, O. E. *J. Chem. Phys.* **1974**, 60, 998.
- (19) Mogensen, O. E. *Appl. Phys.* **1975**, 6, 315.
- (20) Eldrup, M.; Vehanen, A.; Schultz, P. J.; Lynn, K. G. *Phys. Rev. Lett.* **1983**, 51, 2007.
- (21) Mogensen, O. E. *Phys. Lett.* **1983**, 96A, 250.
- (22) Hirata, K.; Kobayashi, Y.; Ujihira, Y. *J. Chem. Soc., Faraday Trans.* **1996**, 92, 985.
- (23) McGervey, J. D.; Yu, Z.; Jamieson, A. M.; Simha, R. *Mater. Sci. Forum* **1995**, 175–178, 727.
- (24) Baugher, A. H.; Kossler, W. J.; Petzinger, K. G. *Macromolecules* **1996**, 29, 7280.
- (25) Baugher, A. H.; Kossler, W. J.; Petzinger, K. G.; Pater, R. H. *Mater. Sci. Forum* **1997**, 255–257, 57.
- (26) Gidley, D. W.; Rich, A.; Sweetman, E.; West, D. *Phys. Rev. Lett.* **1982**, 49, 525.
- (27) Xie, L.; DeMaggio, G. B.; Frieze, W. E.; DeVries, J.; Gidley, D. W.; Hristov, H. A.; Yee, A. F. *Phys. Rev. Lett.* **1995**, 74, 4947.
- (28) Tao, S. J. *J. Chem. Phys.* **1972**, 56, 5499.
- (29) Eldrup, M.; Lighbody, D.; Sherwood, J. N. *Chem. Phys.* **1981**, 63, 51.
- (30) Wang, Y. Y.; Nakanishi, Y.; Jean, Y. C.; Sandreczki, T. C. *J. Polym. Sci., Part B* **1990**, 28, 1431.
- (31) Ito, K.; Nakanishi, H.; Ujihira, Y. *J. Phys. Chem. B* **1999**, 103, 4555.
- (32) Provencher, S. W. *EMBL Technical Report DA05*, European Molecular Biology Laboratory, Germany 1982; *Comput. Phys. Commun.* **1982**, 27, 229.
- (33) Gregory, R. B.; Zhu, Y. *Nucl. Instrum. Methods A* **1990**, 290, 172.
- (34) Marshall, D. B. *Anal. Chem.* **1989**, 61, 660.
- (35) Shukla, A.; Peter, M.; Hoffmann, L. *Nucl. Instrum. Methods A* **1993**, 335, 310.
- (36) Mills, A. P., Jr. *Phys. Rev. Lett.* **1978**, 41, 1828.
- (37) Soininen, E.; Schwab, A.; Lynn, K. G. *Phys. Rev. B* **1991**, 43, 10051.
- (38) Gessmann, Th.; Petkov, M. P.; Weber, M. H.; Lynn, K. G.; Rodbell, K. P.; Asoka-Kumar, P.; Stoeffl, W.; Howell, R. H. *Mater. Sci. Forum* **2001**, 363–365, 585.
- (39) Szpala, S. Ph.D. Dissertation. City College, City University of New York, New York, 1999.
- (40) Szpala, S.; Petkov, M. P.; Lynn, K. G. *Rev. Sci. Instrum.* **2001**, 73, 147.
- (41) Present authors. Unpublished data. The refractive index is a linear function of the porogen load; its slope is compared to that given by the values for MSSQ and air (100% porosity).
- (42) Arguments are given in most introductory books on percolation theory. For example, see: Sahimi, M. *Applications of Percolation Theory*; Taylor & Francis: London, 1994.
- (43) Makhov, A. F. *Sov. Phys. Solid State* **1960**, 2, p 1934; p 1942; p 1945.
- (44) Valkealahti, S.; Nieminen, R. *Appl. Phys. A* **1983**, 32, 95.
- (45) Data on 3γ -annihilation in SiO₂ are rarely published. Exceptions can be found in: Uedono, A.; Wei, L.; Tanigawa, S.; Suzuki, R.; Ohgaki, H.; Mikado, T.; Kawano, T.; Ohji, Y. *J. Appl. Phys.* **1994**, 75, 3822; and Petkov, M. P. Ph.D. Dissertation. Washington State University, Pullman, WA, 1998.
- (46) van Veen, A.; Schut, H.; de Vries, J.; Hakvoort, R. A.; Ijpma, M. R. In *Positron Beams for Solids and Surfaces*; Schultz, P. J., Massoumi, G. R., Simpson, P. J., Eds.; AIP Conference Proceedings No. 218; New York, 1990; p 171.
- (47) Gregory, R. B. *J. Appl. Phys.* **1991**, 70, 4665.
- (48) Dannefaer, S.; Kerr, D.; Craigen, D.; Bretagnon, T.; Taliercio, T.; Foucaran, A. *J. Appl. Phys.* **1996**, 79, 9110.
- (49) Dlubek, G.; Hübner, Ch.; Eichler, S. *Nucl. Instrum. Methods B* **1998**, 142, 191.
- (50) Kansy, J. *Nucl. Instrum. Methods A* **1996**, 374, 235.
- (51) Huang, E.; Toney, M. Private communications.
- (52) Kondoh, E.; Baklanov, M. R.; Lin, E.; Gidley, D.; Nakashima, A. *Jpn. J. Appl. Phys.* **2001**, 40, L323.
- (53) Asoka-Kumar, P.; Leung, T. C.; Lynn, K. G.; Nielsen, B.; Forcier, M. P.; Weinberg, Z. A.; Rubloff, G. W. *J. Appl. Phys.* **1992**, 71, 5606.
- (54) Saito, H.; Hyodo, T. *Phys. Rev. B* **1999**, 60, 11070.
- (55) Mogensen, O. E. *Positron annihilation in chemistry*; Goldanskii, V. I., Schäfer, F. P., Toennies, J. P., Lotsch, H. K. V., Eds.; Springer-Verlag: Berlin, 1995.
- (56) Present authors. Unpublished data.
- (57) Eldrup, M.; Vehanen, A.; Schultz, P. J.; Lynn, K. G. *Phys. Rev. B* **1985**, 32, 7048.